

Article

Pyroelectric Nanogenerator Based on an SbSI–TiO₂ Nanocomposite

Krystian Mistewicz 

Institute of Physics—Center for Science and Education, Silesian University of Technology, Krasińskiego 8, 40-019 Katowice, Poland; krystian.mistewicz@polsl.pl; Tel.: +48-32-603-41-56

Abstract: For the first time, a composite of ferroelectric antimony sulfide (SbSI) nanowires and non-ferroelectric titanium dioxide (TiO₂) nanoparticles was applied as a pyroelectric nanogenerator. SbSI nanowires were fabricated under ultrasonic treatment. Sonochemical synthesis was performed in the presence of TiO₂ nanoparticles. The mean lateral dimension $d_a = 68(2)$ nm and the length $L_a = 2.52(7)$ μm of the SbSI nanowires were determined. TiO₂ nanoparticles served as binders in the synthesized nanocomposite, which allowed for the preparation of dense films via the simple drop-casting method. The SbSI–TiO₂ nanocomposite film was sandwiched between gold and indium tin oxide (ITO) electrodes. The Curie temperature of $T_C = 294(2)$ K was evaluated and confirmed to be consistent with the data reported in the literature for ferroelectric SbSI. The SbSI–TiO₂ device was subjected to periodic thermal fluctuations. The measured pyroelectric signals were highly correlated with the temperature change waveforms. The magnitude of the pyroelectric current was found to be a linear function of the temperature change rate. The high value of the pyroelectric coefficient $p = 264(7)$ nC/(cm²·K) was determined for the SbSI–TiO₂ nanocomposite. When the rate of temperature change was equal $dT/dt = 62.5$ mK/s, the maximum and average surface power densities of the SbSI–TiO₂ nanogenerator reached 8.39(2) and 2.57(2) μW/m², respectively.

Keywords: antimony sulfide; titanium dioxide; nanowires; pyroelectric effect; nanogenerator; renewable energy



Citation: Mistewicz, K. Pyroelectric Nanogenerator Based on an SbSI–TiO₂ Nanocomposite. *Sensors* **2022**, *22*, 69. <https://doi.org/10.3390/s22010069>

Academic Editors: Slim Naifar, Olfa Kanoun and Carlo Trigona

Received: 4 November 2021

Accepted: 21 December 2021

Published: 23 December 2021

Publisher's Note: MDPI stays neutral with regard to jurisdictional claims in published maps and institutional affiliations.



Copyright: © 2021 by the author. Licensee MDPI, Basel, Switzerland. This article is an open access article distributed under the terms and conditions of the Creative Commons Attribution (CC BY) license (<https://creativecommons.org/licenses/by/4.0/>).

1. Introduction

Efficiency in thermal energy harvesting is an important challenge to produce green energy for sustainable development. Most of the waste heat generated in industry is available at low temperatures, generally below 373–503 K [1]. Low-temperature waste heat is especially difficult to recover successfully using currently available technologies [2]. Thermal energy can be converted into electric energy by applying electrochemical systems [3], thermogalvanic cells [4,5], thermoelectric [6–8], thermomagnetic [9,10], and pyroelectric generators [11–13]. However, all mentioned technologies suffer from low efficiency and limited reliability. Therefore, new materials and engineering concepts must be proposed and developed in the field of low-temperature waste heat recovery to ensure their future large-scale and commercial application.

Inorganic ferroelectric crystals or ceramics [14,15], ferroelectric polymers [16], and non-ferroelectric compounds [17] are three main groups of materials commonly used to construct pyroelectric generators. Material morphology is a key factor affecting the pyroelectric performance of the device. The efficiency of thermal energy conversion to electrical power can be enhanced through quantum confinement in pyroelectric nanomaterials [18]. Thus, there is growing interest in the development and examination of pyroelectric nanogenerators based on thin films [19], nanowires [20,21], or nanoparticles [22].

Antimony sulfide (SbSI) is a ternary compound that possesses ferroelectric properties with a Curie temperature of 295 K [23]. The first report on the pyroelectric properties of SbSI single crystals was provided by Imai et al. [24]. The large pyroelectric coefficient (1.2 μC/(cm²·K)) of bulk single crystals of SbSI was measured over a temperature range

encompassing the ferroelectric phase transition [25]. The significantly much lower pyroelectric coefficients of $8.06 \text{ pC}/(\text{cm}^2 \cdot \text{K})$ and $180 \text{ nC}/(\text{cm}^2 \cdot \text{K})$ were determined for SbSI films grown by flash evaporation [26] and physical vapor deposition [27], respectively. However, the pyroelectric properties of SbSI nanowires have not been investigated so far. Recently, nanowires of SbSI and other compounds that belong to the chalcogenide family of materials have received a great amount of attention due to the fact of their possible applications in piezoelectric nanogenerators for mechanical energy harvesting [28,29], underwater ultrasounds sensors [30], photovoltaic devices [31,32], piezo- and photocatalysis [33,34].

Many different techniques have been proposed till now to fabricate antimony sulfide films including electron beam evaporation [35], flash evaporation [36,37], physical vapor deposition [27], pulsed laser deposition [38,39], molecular beam epitaxy [40], solution processing [41], and combined solution and vapor processes [42,43]. The majority of the aforementioned techniques possess serious drawbacks such as complexity or the need to use high-temperature treatments. A typical way to fabricate continuous films of SbSI nanowires is based on the application of a binding polymer matrix, e.g., polyacrylonitrile (PAN) [32]. As a result, the electrical properties of such a prepared composite can be worse in comparison to the electrical properties of pristine SbSI nanowires. Ye and co-workers [44] presented sol-gel fabrication of thin films and bulk solids of SbSI micro-crystallite-doped organically modified TiO_2 . The optical absorption spectrum of this material exhibited an evident quantum confinement effect [44], whereas the electrical properties of the material were not examined. It should be noted that the application of TiO_2 nanoparticles in composites for pyroelectric nanogenerators has been reported in the literature as a factor improving pyroelectric performance [45].

In this paper, a facile fabrication of the SbSI- TiO_2 nanocomposite in one step is presented for the first time. TiO_2 nanoparticles were used as binders in the synthesized nanocomposite. The dense film of the SbSI- TiO_2 nanocomposite was prepared using a simple drop-casting method and sandwiched between the electrodes. Such a device was applied as a pyroelectric nanogenerator.

2. Materials and Methods

2.1. Material Synthesis and Nanogenerator Fabrication

Figure 1 presents the preparation of the pyroelectric nanogenerator. In the first stage, the chemical elements (i.e., antimony, sulfur, and iodine) were weighted in a stoichiometric ratio. The reagents (i.e., 868 mg of Sb, 227 mg of S, and 921 mg of I_2) were mixed with titanium dioxide (TiO_2) nanoparticles purchased from Merck KGaA. According to the data provided by the material manufacturer, the average size of the TiO_2 nanoparticles was 21 nm. The mass of TiO_2 (860 mg) was adjusted to constitute approximately 30% of the total mass of the nanocomposite. The mixture was added to the beaker containing 10 mL of pure ethanol (Figure 1a). Such a prepared suspension of the reagents was subjected to ultrasonic irradiation, generated by the VCX-750 ultrasonic reactor (Sonics & Materials, Inc., Newtown, CT, USA) as shown in Figure 1b. The material synthesis was carried out at a temperature of 323 K over 4 h. After the synthesis was completed, the orange gel of the SbSI- TiO_2 nanocomposite was drop-casted onto an indium tin oxide (ITO) coated polyethylene terephthalate (PET) substrate as depicted in the Figure 1c. The drop-casting deposition of the material was performed in several steps using an electronic pipette. The sample was then placed on a hot plate and dried at a temperature of 333 K (Figure 1d). When the sample drying was finished, the 200 nm thick gold electrode was sputtered on the top side of the SbSI- TiO_2 nanocomposite (Figure 1e) by applying a Q150R ES rotary pumped coater (Quorum Technologies Ltd., Laughton, United Kingdom). Finally, the prepared SbSI- TiO_2 nanogenerator was connected to the external measurement circuit (Figure 1f).

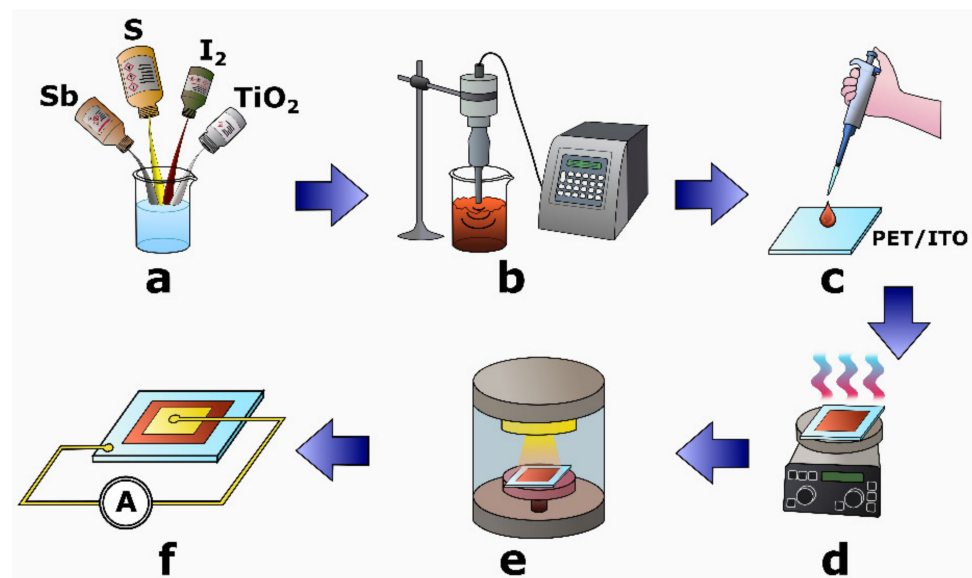


Figure 1. Schematic fabrication process flow of the SbSI-TiO₂ pyroelectric nanogenerator. A detailed description is given in the text.

2.2. Structural and Chemical Characterization of the SbSI-TiO₂ Nanocomposite

The morphology and chemical composition of the SbSI-TiO₂ nanocomposite were investigated using scanning electron microscopy (SEM) and energy-dispersive X-ray spectroscopy (EDS), respectively. The experiments were performed using a Phenom Pro X microscope (Thermo Fisher Scientific, Waltham, MA, USA) integrated with an EDS spectrometer. The SEM studies were carried out at the acceleration voltage of 10 kV, whereas the EDS survey was accomplished at 15 kV. The EDS data were analyzed using the ProSuite Element Identification computer program (Thermo Fisher Scientific).

2.3. Electrical Measurements

The SbSI-TiO₂ nanocomposite was inserted into the SH-242 environmental test chamber (Espec) to examine its electrical properties. All experiments were carried out at a constant relative humidity (RH) of 50%. The sample was tested under dark conditions to eliminate the influence of excess carriers photogeneration on the measured electric signals. The change in temperature was achieved via air flow inside the chamber. The measurements were performed at a standard atmospheric pressure (1 atm). It was confirmed for the SbSI nanowires that their electrical properties are sensitive to the various gases including oxygen and hydrogen [46]. However, the air circulation inside the chamber was closed. Thus, the gas composition of the air remained the same. As a result, the effect of the gas on the electrical properties of the sample was eliminated. Before pyroelectric investigations, the SbSI-TiO₂ nanocomposite was poled to align the electric dipoles in the SbSI nanowires and enhance the pyroelectric output of the nanogenerator. It was conducted by cooling the device below the Curie temperature and applying an external electric field of 12 kV/m, which is higher than the coercive field of SbSI [23]. The pyroelectric response of the SbSI-TiO₂ nanocomposite was registered for different rates of temperature change (dT/dt) in the range from 1.8 to 62.5 mK/s. The low values of dT/dt were chosen to avoid possible interference caused by the thermoelectric effect [47]. The electric output of the SbSI-TiO₂ nanocomposite was measured with the 6430 Sub-Femtoamp Remote SourceMeter (Tektronix, Beaverton, OR, USA). Data acquisition was performed using a PC computer with a GPIB bus and an appropriate program in LabView (National Instruments, Austin, TX, USA).

3. Results and Discussion

Figure 2a presents the prepared pyroelectric nanogenerator based on the SbSI–TiO₂ nanocomposite sandwiched between the Au electrode and ITO-coated PET. A typical SEM micrograph of the SbSI–TiO₂ nanocomposite is shown in Figure 1b. This material consisted of randomly distributed one-dimensional nanocrystals of SbSI and agglomerations of TiO₂ nanoparticles. The concentrations of the chemical elements were averaged over the sample. The EDS survey proved that titanium dioxide constituted 29.9% of the total mass of the nanocomposite, which is in good agreement with the initial amount of TiO₂ (30%) used for material preparation. TiO₂ nanoparticles served as fillers in the synthesized nanocomposite, which allowed for preparing dense films via a facile drop-casting method. Many attempts have been made to fabricate films containing only SbSI nanowires. However, they were not successful. The presence of voids in the layers of pure SbSI nanowires (without TiO₂ nanoparticles) resulted in the formation of the short-circuited samples after sputtering of the gold electrodes. Another way to fabricate a continuous film of SbSI nanowires is by applying a polymer as a binder [32]. Such a method possesses a significant drawback. It was found in [32] that the increase in polymer concentration in the SbSI–PAN nanocomposite led to an undesirable reduction in its electrical conductivity and photovoltaic performance.

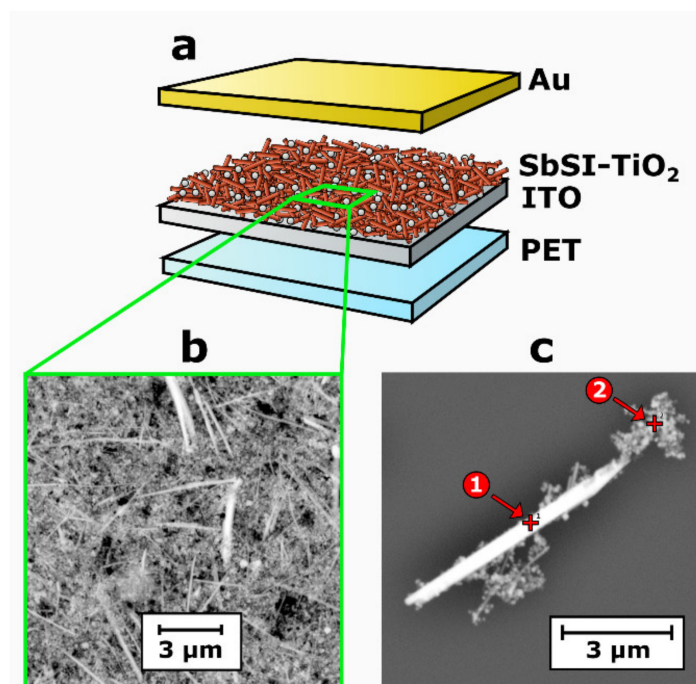


Figure 2. The layer structure of the pyroelectric nanogenerator (a), SEM micrograph of the SbSI–TiO₂ film (b), and a selected nanowire (c).

The elemental atomic ratio of 0.37:0.36:0.27 for Sb, S, and I averaged over nanocomposite volume was close to the stoichiometric composition of SbSI (Table 1). The theoretical values should be 0.33 for each of the elements in this ternary compound. No other elements were detected in the sample. The small amount of material was deposited on the Si substrate. An individual SbSI nanowire was separated from the nanocomposite to examine its chemical composition (Figure 2c). The EDS signal for Si was subtracted from the atomic concentrations evaluated for other components. The elemental atomic ratio registered for spot 1 in Figure 2c corresponded to the chemical composition expected for antimony sulfiodide (Table 1). The values of atomic concentrations determined for spot 2 in Figure 2c indicate the presence of agglomerated TiO₂ nanoparticles and slight traces of antimony. It should be noted that an excess amount of Sb is frequently reported in the literature for nanowires [32,34], nanocrystals [33], and thin films [27] of SbSI. This effect

can be attributed to the fact that the surface of crystalline SbSI nanowires is surrounded by fuzzy shells, which have a chemical composition that may be different from the concentrations of elements in the core of the nanowire [32]. Atomic concentrations of titanium and oxygen are in agreement with the theoretical values for stoichiometric TiO₂ (Table 1). Since titanium dioxide exhibits excellent chemical stability [48,49], it should be resistant to ultrasonic treatment.

Table 1. The chemical composition determined for the areas of the sample shown in Figure 2b,c.

Chemical Element	Atomic Concentration, %		
	Area in Figure 2b	Spot 1 in Figure 2c	Spot 2 in Figure 2c
Sb	15.6	36.8	13.8
S	14.9	30.4	0
I	11.1	32.8	0
Ti	18.5	0	28.8
O	39.9	0	57.4

The prepared material was characterized with scanning electron microscopy to determine the average diameter and length of the SbSI nanowires as presented in Figure 3. Manual image analysis was performed on 250 randomly selected nanowires. The diameters and lengths vary in the wide ranges, reaching up to 220 nm and 8.2 μm, respectively. One can see that the distribution of nanowires sizes followed a log-normal function [50,51]:

$$f(x) = \frac{A}{\sqrt{2\pi} \cdot \sigma \cdot x} \exp \left[-\frac{\left[\ln \left(\frac{x}{x_a} \right) \right]^2}{2\sigma^2} \right], \quad (1)$$

where A is a constant, x means the size of the nanowires (diameter or length), x_a denotes the average value of the nanowire size, and σ is its standard deviation. It should be underlined that the log-normal function is frequently reported in the literature as a relation describing size distributions of nanowires [50–52] and nanoparticles [53–55]. The mean diameter $d_a = 68(2)$ nm and the length $L_a = 2.52(7)$ μm of the SbSI nanowires were determined. The obtained value of d_a is equal within the measurement uncertainty to the average diameter (69(3) nm) of the SbSI nanowires reported in [32].

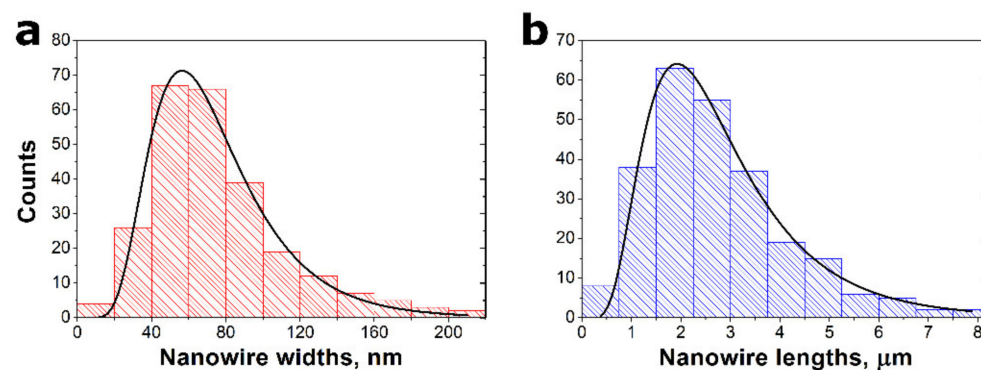


Figure 3. Distributions widths (a) and lengths (b) of SbSI nanowires in the SbSI–TiO₂ nanocomposite. The black lines represent log-normal functions expected for the nanoscale object size distribution described by Equation (1). The values of the fitted parameters of Equation (1) are given in the text.

The influence of temperature on the electric current flowing through the SbSI–TiO₂ nanocomposite under constant bias voltage is shown in Figure 4a. The rise in temperature leads to a sharp enhancement of the electric current. It is a typical behavior for a semiconducting material. Moreover, when the temperature increases, the reduction in the grain boundary resistance can result in the reduction in the barrier for the mobility of charge

carriers participating in grain boundary conduction [56]. Taking into account the geometrical dimensions of the investigated sample, the electric conductance of the SbSI–TiO₂ nanocomposite was calculated (Figure 4b). It is well known that in the case of ferroelectric material, the Arrhenius plot of an electric conductance consists of two linear curves with different slopes corresponding to the paraelectric and ferroelectric phases [56,57]. Thus, a change in activation energy is observed near Curie temperature (T_C) [58–60]. This effect was also documented in the literature for thin films of SbSI [35,61]. Two different theoretical curves were least squares fitted to the experimental results, shown in Figure 4b, using a well-known relation [56,57]:

$$\sigma(T) = \sigma_0 \cdot \exp\left(-\frac{E_A}{k_B T}\right), \quad (2)$$

where σ_0 is the pre-exponential coefficient, E_A means an activation energy, and k_B denotes the Boltzmann constant. The values of activation energies of $E_A = 0.537(1)$ eV and $E_A = 0.271(2)$ eV were determined for the paraelectric and ferroelectric phases, respectively. They could not be compared with the literature data for SbSI due to the fact that these parameters are thickness dependent [61]. Finding the intersection of the linear dependencies in the Arrhenius plot of an electric conductance (Figure 4b) allowed for the estimation of the Curie temperature of the examined material ($T_C = 294(2)$ K). The obtained value was consistent with the data from the literature for ferroelectric SbSI listed in Table 2.

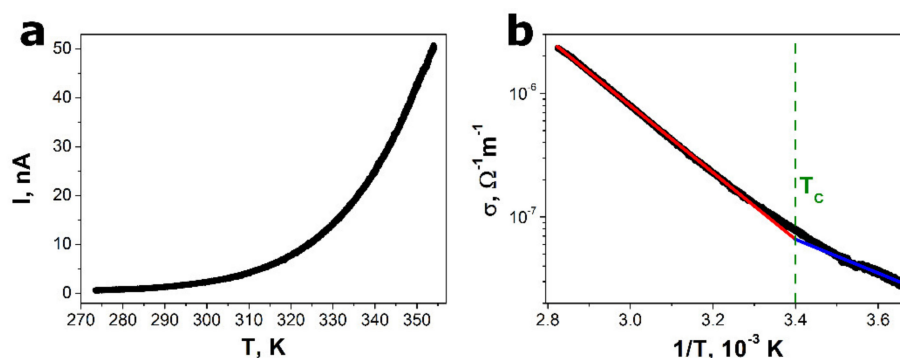


Figure 4. The temperature dependence of the electric current registered under a constant bias voltage of 0.1 V (a) and the Arrhenius plot electrical conductance of the SbSI–TiO₂ nanocomposite (b). The solid red and blue lines in (b) represent the best fitted theoretical dependence (2) in the paraelectric and ferroelectric phases, respectively. The green, dashed line indicates the reciprocal value of the determined Curie temperature. The values of the fitted parameters of Equation (2) are given in the text.

Table 2. A comparison of the determined Curie temperature of the SbSI–TiO₂ nanocomposite with literature data for SbSI.

Material	Preparation Method	T_C , K	Reference
bulk crystal of SbSI		295	[23]
bulk crystal of SbSI	vapor phase growth	292–293	[24]
bulk crystal of SbSI	Bridgman method and vapor transport technique	293	[25]
SbSI film	physical vapor deposition	295	[27]
SbSI film	electron beam evaporation	294	[35]
SbSI film	flash evaporation	293	[37]
SbSI film	pulsed laser deposition	292	[38]
SbSI film	pulsed laser deposition	290–294	[39]
SbSI nanowires	sonochemical synthesis	291(2)	[62]
SbSI–TiO ₂ nanocomposite	sonochemical synthesis	294(2)	this paper

The sample of the SbSI–TiO₂ nanocomposite was subjected to periodic temperature fluctuations as presented in Figure 5a,c. The experiments were performed for different amplitudes of temperature changes. A rectangular-shaped transient characteristic of pyroelectric current was observed (Figure 5b,d) when the triangular temperature waveform was applied to the SbSI–TiO₂ nanogenerator. Such behavior is well documented in the literature for other pyroelectric materials, e.g., PVDF–TiO₂ composite [45], PVDF–ZnO nanocomposite [63], Bi_{0.5}Na_{0.5}TiO₃–P(VDF–TrFE) nanocomposite [64], P(VDF–TrFE) [65], PbTiO₃–P(VDF–TrFE) [66], LiNbO₃–polypropylene [67], CeO₂-doped Na_{0.5}Bi_{0.5}TiO₃ ceramics [68], BaZr_{0.2}Ti_{0.8}O₃/Ba_{0.7}Ca_{0.3}TiO₃ heterostructures [69], and CdS nanorods [47]. This proves that the measured electric response of the SbSI–TiO₂ nanocomposite was due to the true pyroelectric effect. It should be noted that only SbSI nanowires contributed to the pyroelectric response of the nanocomposite. The non-ferroelectric inclusion of TiO₂ cannot be polarized, since its net dipole moment is almost zero [45]. A slight decrease in the amplitude of the pyroelectric response, shown in Figure 5d, can be attributed to the so-called “aging effect” [70].

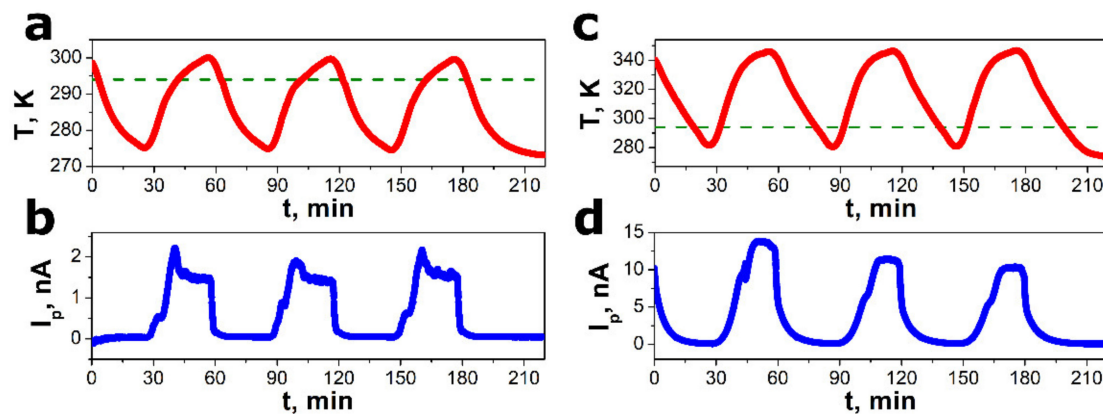


Figure 5. Cyclic changes in temperature (a,c) and corresponding output current (b,d) of the SbSI–TiO₂ pyroelectric nanogenerator. The green horizontal line represents the value of the Curie temperature $T_C = 294(2)$ K.

The only positive pyroelectric response of the SbSI–TiO₂ nanogenerator is observed (Figure 5b,d) due to the fact that the rectifying *p–n* heterojunction was formed between the SbSI nanowires and the ITO electrode as well between the SbSI nanowires and the TiO₂ nanoparticles. Usually, SbSI is regarded as *p*-type semiconductor [31,37,61,71,72], whereas both ITO [73] and TiO₂ [74] exhibit *n*-type electrical conductivity. The work functions of ITO, TiO₂, and SbSI were 4.4–4.5 eV [75], 4.2–4.7 eV [76], and 5 eV [31,71,72], respectively. Accordingly, since the work function of *p*-type SbSI is higher than that of *n*-type ITO and *n*-type TiO₂, a built-in electric field was formed in the ITO/SbSI and TiO₂/SbSI interfaces. When the temperature increased ($dT/dt > 0$), a positive pyroelectric potential was formed. Thus, the ITO/SbSI and TiO₂/SbSI interfaces were forward-biased pn junctions. In such a case, the electrons could flow freely across the interfaces, and the pyroelectric current was measured in the external circuit. When the device cooled down ($dT/dt < 0$), the ITO/SbSI and TiO₂/SbSI interfaces were reversely biased barriers, leading to almost zero electric output of the nanogenerator. This is the process of creating, separating, preserving, and accumulating charges [77]. As a result, the device generated a rectified electric output. The same effect is observed in the case of direct-current generators based on *p–n* [78–82] or Schottky [77,83–85] junctions. Morozovska et al. [20] proposed that the rectification effect of the junction barrier allows the application of a ferroelectric nanowire array fixed between flat electrodes as the direct current generator. Moreover, one should remember that the built-in electrical field of a *p–n* junction barrier can create a polar axis in the solid [86]. The pyroelectric effect can be enhanced, as the electric dipole moment, due to the charge

separation at the junction, depending on the temperature mainly through the temperature dependence of the dielectric constant [86].

The magnitude of the pyroelectric current depends on the rate of temperature change (dT/dt). It is described by the following equation [11–13]:

$$I_p = \frac{dQ}{dt} = pA \frac{dT}{dt}, \quad (3)$$

where Q represents a pyroelectric charge, p denotes the pyroelectric coefficient, and A means the electrode area. The pyroelectric current density ($J_p = I_p/A$) is presented as a function of the rate of temperature change in Figure 6a. One can see that the experimental results followed a linear dependence. According to Equation (3), the slope of J_p versus dT/dt was equal to the pyroelectric coefficient. The value of the pyroelectric coefficient of $p = 264(7) \text{ nC}/(\text{cm}^2 \cdot \text{K})$ was determined for the SbSI–TiO₂ nanocomposite by fitting the theoretical Formula (3) to the experimental data in the graph in Figure 6a.

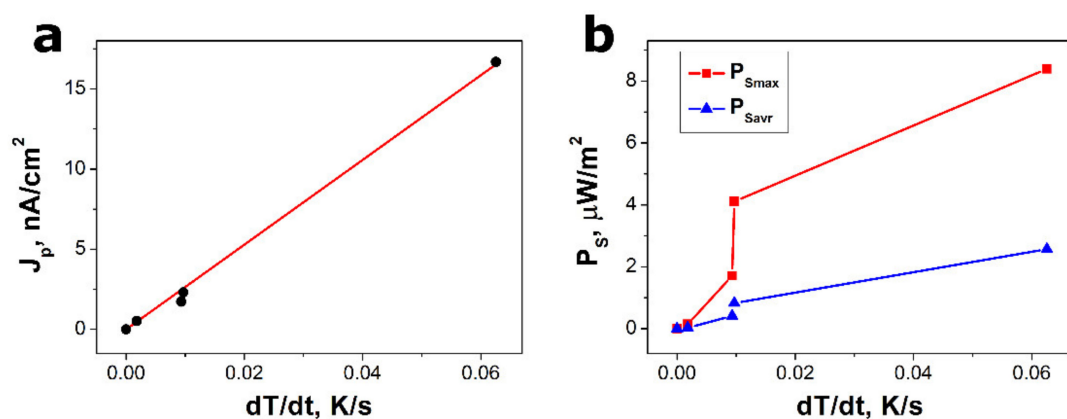


Figure 6. The output pyroelectric current density (a) and the surface power density (b) of the SbSI–TiO₂ pyroelectric nanogenerator as a function of the temperature change rate. The red line in Figure (a) represents the best fit dependence (3). The red and blue experimental points in Figure (b) show the values of the maximum and average surface power density, respectively.

The maximum power density (P_{Smax}) of the SbSI–TiO₂ nanogenerator was calculated using the peak values of the output pyroelectric current (I_{pmax}), voltage (U_{max}), and electrode area of the device (A):

$$P_{Smax} = \frac{U_{max} \cdot I_{pmax}}{A}. \quad (4)$$

One can see that the maximum surface power density is proportional to the maximum value of the pyroelectric current density. The average values of the surface power density (P_{Savr}) were determined using the following equation:

$$P_{Savr} = \frac{P_{avr}}{A} = \frac{1}{A \cdot \Delta t} \cdot \int_0^{\Delta t} U \cdot I_p dt, \quad (5)$$

where Δt represents the period time of a heating–cooling cycle. Figure 6b shows that the increase in the temperature change rate resulted in the obvious rise of P_{Smax} and P_{Savr} . The pyroelectric coefficient, the maximum and average power densities, calculated for the SbSI–TiO₂ nanocomposite, were compared with the values of these parameters reported in the literature for other pyroelectric materials (Table 3). They were divided into five main groups, i.e., non-ferroelectric materials, inorganic ferroelectric bulk crystals or ceramics, pure ferroelectric polymers, ferroelectric thin films or nanomaterials, and ferroelectric composites. It should be underlined that the SbSI–TiO₂ nanocomposite had the highest values for the pyroelectric coefficient and surface power density among all the ferroelectric

composites as listed in Table 3. Furthermore, the pyroelectric performance of the SbSI–TiO₂ nanocomposite was much better than that achieved for the thin films of SbSI [26,27] and nanowires of antimony seleniodide (SbSeI) [87], which is an isostructural material for SbSI [88]. It is expected that the incomplete coverage of the TiO₂ on the SbSI nanorods should lead to the formation of pores between these two different materials. A matrix–void composite with low permittivity is desired for pyroelectric applications, exhibiting a high figure of merit [89,90]. Therefore, the high pyroelectric performance of the SbSI–TiO₂ nanocomposite can be attributed to the good pyroelectric properties of SbSI as well as to the incomplete coverage of the TiO₂ on the SbSI nanorods.

Table 3. Comparison of the pyroelectric performance achieved for the SbSI–TiO₂ nanocomposite and other materials (BCs—bulk ceramics; BNT—Bi_{0.5}Na_{0.5}TiO₃; NPs—nanoparticles; NRs—nanorods; NWs—nanowires; *p*—pyroelectric coefficient; *P_S*—surface power density; PVC—poly(vinyl chloride); PVDF polyvinylidene difluoride; P(VDF–TrFE)—poly(vinylidene fluoride-co-trifluoroethylene); PZT—lead zirconate titanate; SC—single crystal; TFs—thin films). The abbreviations “max” and “avr” refer to the maximum and average surface power densities, respectively.

Group of Materials	Material	<i>p</i> , nC/(cm ² ·K)	<i>P_S</i> , μW/m ²	Reference
non-ferroelectric materials	ZnO NWs	1.5		[91]
	ZnO TFs	1.0–1.4		[92]
	CdS NRs	470		[47]
inorganic ferroelectric bulk crystals or ceramics	PZT BCs	53.3	3700 ^{max}	[93]
	PZT BCs	20	13.6 ^{avr}	[94]
	BaTiO ₃ BCs	10	2240 ^{max}	[95]
	BaTiO ₃ BCs	16		[96]
	LiNbO ₃ SC	5–8	219 ^{max}	[97]
	SbSI SC	1200		[25]
pure ferroelectric polymers	PVDF	1.94		[45]
	PVDF	4	108 ^{max}	[98]
	PVDF		0.13 ^{max}	[99]
	P(VDF–TrFE)	2.4		[65]
	P(VDF–TrFE)	4.39	128 ^{max}	[100]
ferroelectric thin films or nanomaterials	Ba _{0.8} Sr _{0.2} TiO ₃ TFs	25		[101]
	KNbO ₃ NWs	0.8		[102]
	SbSI TFs	0.008		[26]
	SbSI TFs	180		[27]
	SbSeI NWs	44(5)	0.59(4) ^{max}	[87]
ferroelectric composites	BaTiO ₃ –PVC	10.6		[103]
	PVDF–diamond NPs	8.7		[104]
	PVDF–TiO ₂	2.45		[45]
	PVDF–ZnO NPs	~2.9		[63]
	PVDF–CH ₃ NH ₃ PbI ₃	0.004	1.75 ^{max}	[105]
	P(VDF–TrFE)–BNT NPs	5		[64]
	P(VDF–TrFE)–PbTiO ₃ NPs	4		[66]
	SbSI NWs–TiO ₂ NPs	264(7)	8.39(2) ^{max} 2.57(2) ^{avr}	this paper

Electrical energy (ΔE_V) generated by a unit of the volume (V) of the SbSI–TiO₂ nanocomposite during the time interval (t) was evaluated applying a formula given below:

$$\Delta E_V = \frac{1}{V} \cdot \int_0^t U \cdot I_p dt. \quad (6)$$

Figure 7 presents a time dependence of the volume energy density generated by the SbSI–TiO₂ device during three periodic thermal input cycles. An increase in the rate of temperature change leads to an enhancement of the ΔE_V . When the temperature difference (ΔT) was equal to 25 K, the electrical energy produced per unit volume of the

SbSI–TiO₂ nanocomposite per cycle amounted to 15.2 $\mu\text{J}/\text{cm}^3$. This value was lower than $\Delta E_V = 230 \mu\text{J}/\text{cm}^3$ achieved for the PVDF film per single thermal cycle at the temperature change $\Delta T = 23 \text{ K}$ [93].

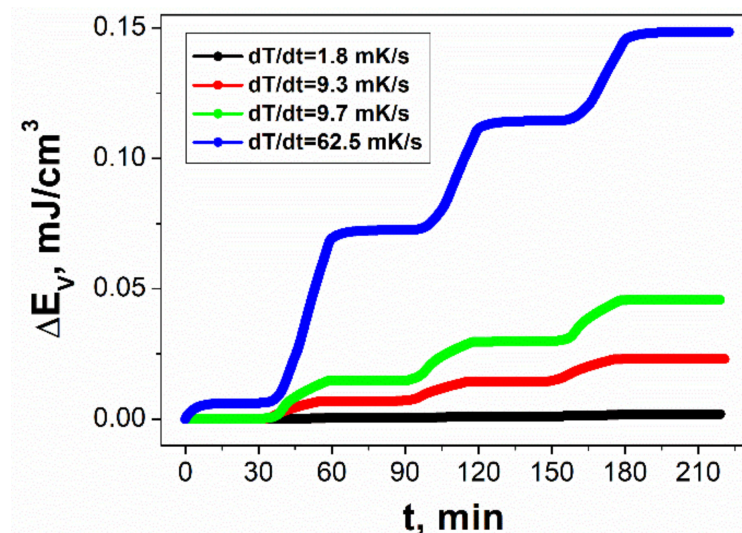


Figure 7. Volume energy density generated by the SbSI–TiO₂ device during three periodic thermal input cycles measured for different rates of temperature change (● 1.8 mK/s; ● 9.3 mK/s; ● 9.7 mK/s; ● 62.5 mK/s).

The probable impact of the size of the TiO₂ nanoparticles on the pyroelectric efficiency of the SbSI–TiO₂ nanocomposite can be explained as follows. A decrease in a TiO₂ nanoparticle's size leads to a reduction in the electrical conductivity of this nanomaterial [106]. Wei and co-workers [107] presented that lower conductivity of the ceramic inclusion in the ferroelectric composite results in higher polarization, which is favorable to the poling of the composite. Therefore, the enhancement of the pyroelectric performance of the SbSI–TiO₂ nanocomposite should be observed with the decrease of the TiO₂ nanoparticle's size.

4. Conclusions

For the first time, a method of fabrication of the SbSI–TiO₂ pyroelectric nanogenerator was described. It involved the sonochemical preparation of the SbSI–TiO₂ nanocomposite in a single step and its drop-casting deposition on ITO-coated PET. TiO₂ nanoparticles served as fillers in the synthesized nanocomposite, which were crucial to obtain dense films with the desired morphology. It is a new alternative approach to fabricate devices based on nanowires. This method eliminates the need for application of a polymer matrix as a binder. The proposed technology is simple and universal. It can be used for preparation of nanogenerators from other one-dimensional chalcogenide nanostructures.

The SEM and EDS studies of the SbSI–TiO₂ nanocomposite confirmed the formation of stoichiometric SbSI nanowires with an average diameter and length of 68(2) nm and 2.52(7) μm , respectively. The Curie temperature of 294(2) K was determined for the examined material, which is in good agreement with the data reported in the literature for ferroelectric bulk crystals, thin films, and pristine nanowires of SbSI.

The SbSI–TiO₂ nanocomposite sandwiched between the ITO and Au electrodes was subjected to periodic temperature fluctuations. The registered pyroelectric response was well correlated to the temperature changes. The measured signal originated from the pyroelectric properties of SbSI nanowires. Non-ferroelectric TiO₂ nanoparticles were unable to contribute to the electric output of the nanogenerator, since they cannot be polarized. The pyroelectric current density was found to be a linear function of the rate of temperature change. The large pyroelectric coefficient of 264(7) $\text{nC}/(\text{cm}^2 \cdot \text{K})$ was determined for the SbSI–TiO₂ nanocomposite. This value was higher than the pyroelectric coefficient reported in the

literature for many different pyroelectric materials including ZnO nanowires, PZT bulk ceramics, BaTiO₃ bulk ceramics, LiNbO₃ single crystal, PVDF polymers, SbSI thin films, and nanowires of SbSeI, which is an isostructural material to the SbSI. The maximum and average surface power densities of the SbSI–TiO₂ nanogenerator reached 8.39(2) and 2.57(2) $\mu\text{W}/\text{m}^2$, respectively. The electrical energy produced per unit volume of 15.2 $\mu\text{J}/\text{cm}^3$ was obtained per one thermal cycle for which the temperature change was equal to 25 K. It is expected that the values of the aforementioned parameters can be enhanced by adjusting the weight concentration of the titanium dioxide in the nanocomposite. Such investigations will be performed in the near future. The results, presented in this paper, demonstrate that the ferroelectric SbSI–TiO₂ nanocomposite has great potential for use in pyroelectric sensors and thermal energy harvesters.

Funding: This paper was partially supported by the Silesian University of Technology (Gliwice, Poland) through the Rector’s pro-quality grant No. 14/010/RGJ21/0006 and Rector’s habilitation grant No. 14/010/RGH21/0008 in the area of scientific research and development.

Institutional Review Board Statement: Not applicable.

Informed Consent Statement: Not applicable.

Conflicts of Interest: The author declares no conflict of interest. The funders had no role in the design of the study; in the collection, analyses, or interpretation of data; in the writing of the manuscript or in the decision to publish the results.

References

- Pandya, S.; Velarde, G.; Zhang, L.; Wilbur, J.D.; Smith, A.; Hanrahan, B.; Dames, D.; Martin, L.W. New approach to waste-heat energy harvesting: Pyroelectric energy conversion. *NPG Asia Mater.* **2019**, *11*, 26. [[CrossRef](#)]
- Xu, Z.Y.; Wang, R.Z.; Yang, C. Perspectives for low-temperature waste heat recovery. *Energy* **2019**, *176*, 1037–1043. [[CrossRef](#)]
- Rahimi, M.; Straub, A.P.; Zhang, F.; Zhu, X.; Elimelech, M.; Gorski, C.A.; Logan, B.E. Emerging electrochemical and membrane-based systems to convert low-grade heat to electricity. *Energy Environ. Sci.* **2018**, *11*, 276–285. [[CrossRef](#)]
- Duan, J.; Feng, G.; Yu, B.; Li, J.; Chen, M.; Yang, P.; Feng, J.; Liu, K.; Zhou, J. Aqueous thermogalvanic cells with a high Seebeck coefficient for low-grade heat harvest. *Nat. Commun.* **2018**, *9*, 5146. [[CrossRef](#)]
- Owusu, M.; Mensah-Darkwa, K.; Andrews, A.; Davis, F.; Phelan, P. Effect of transient low-grade solar heat on liquid thermogalvanic cells. *Mater. Today Proc.* **2021**, *38*, 767–772. [[CrossRef](#)]
- Jaziri, N.; Boughamoura, A.; Müller, J.; Mezghani, B.; Tounsi, F.; Ismail, M. A comprehensive review of Thermoelectric Generators: Technologies and common applications. *Energy Rep.* **2020**, *6*, 264–287. [[CrossRef](#)]
- Zulkepli, N.; Yunas, J.; Ambri Mohamed, M.; Hamzah, A.A. Review of Thermoelectric Generators at Low Operating Temperatures: Working Principles and Materials. *Micromachines* **2021**, *12*, 734. [[CrossRef](#)]
- Zoui, M.A.; Bentouba, S.; Stocholm, J.G.; Bourouis, M. A Review on Thermoelectric Generators: Progress and Applications. *Energies* **2020**, *13*, 3606. [[CrossRef](#)]
- Kishore, R.A.; Priya, S. A Review on Low-Grade Thermal Energy Harvesting: Materials, Methods and Devices. *Materials* **2018**, *11*, 1433. [[CrossRef](#)]
- Kishore, R.A.; Davis, B.; Greathouse, J.; Hannon, A.; Kennedy, D.E.; Millar, A.; Mittel, D.; Nozariasbmarz, A.; Kang, M.G.; Kang, H.B.; et al. Energy scavenging from ultra-low temperature gradients. *Energy Environ. Sci.* **2019**, *12*, 1008–1018. [[CrossRef](#)]
- Ryu, H.; Kim, S.-W. Emerging Pyroelectric Nanogenerators to Convert Thermal Energy into Electrical Energy. *Small* **2019**, *17*, 1903469. [[CrossRef](#)]
- Bowen, C.R.; Taylor, J.; LeBoulbar, E.; Zabek, D.; Chauhan, A.; Vaish, R. Pyroelectric materials and devices for energy harvesting applications. *Energy Environ. Sci.* **2014**, *7*, 3836–3856. [[CrossRef](#)]
- Lingam, D.; Parikh, A.R.; Huang, J.; Jain, A.; Minary-Jolandan, M. Nano/microscale pyroelectric energy harvesting: Challenges and opportunities. *Int. J. Smart Nano Mater.* **2013**, *4*, 229–245. [[CrossRef](#)]
- Lee, F.Y.; Jo, H.R.; Lynch, C.S.; Pilon, L. Pyroelectric energy conversion using PLZT ceramics and the ferroelectric–ergodic relaxor phase transition. *Smart Mater. Struct.* **2013**, *22*, 025038. [[CrossRef](#)]
- Zhang, Y.; Xie, M.; Roscow, J.; Bao, Y.; Zhou, K.; Zhang, D.; Bowen, C.R. Enhanced pyroelectric and piezoelectric properties of PZT with aligned porosity for energy harvesting applications. *J. Mater. Chem. A* **2017**, *5*, 6569–6580. [[CrossRef](#)] [[PubMed](#)]
- Qiu, X. Patterned piezo-, pyro-, and ferroelectricity of poled polymer electrets. *J. Appl. Phys.* **2010**, *108*, 011101. [[CrossRef](#)]
- Hsiao, C.-C.; Yu, S.-Y. Improved Response of ZnO Films for Pyroelectric Devices. *Sensors* **2012**, *12*, 17007–17022. [[CrossRef](#)] [[PubMed](#)]

18. Morozovska, A.N.; Eliseev, E.A.; Glinchuk, M.D.; Shevliakova, H.V.; Svechnikov, G.S.; Silibin, M.V.; Sysa, A.V.; Yaremkevich, A.D.; Morozovsky, N.V.; Shvartsman, V.V. Analytical description of the size effect on pyroelectric and electrocaloric properties of ferroelectric nanoparticles. *Phys. Rev. Mater.* **2019**, *3*, 104414. [[CrossRef](#)]
19. Velarde, G.; Pandya, S.; Karthik, J.; Pesquera, D.; Martin, L.W. Pyroelectric thin films—Past, present, and future. *APL Mater.* **2021**, *9*, 010702. [[CrossRef](#)]
20. Morozovska, A.N.; Eliseev, E.A.; Svechnikov, G.S.; Kalinin, S.V. Pyroelectric response of ferroelectric nanowires: Size effect and electric energy harvesting. *J. Appl. Phys.* **2010**, *108*, 042009. [[CrossRef](#)]
21. Chen, X.; Shao, J.; Li, X.; Tian, H. A Flexible Piezoelectric-Pyroelectric Hybrid Nanogenerator Based on P(VDF-TrFE) Nanowire Array. *IEEE Trans. Nanotechnol.* **2016**, *15*, 295–302. [[CrossRef](#)]
22. Meneses-Franco, A.; Trujillo-Rojo, V.H.; Soto-Bustamante, E.A. Synthesis and characterization of pyroelectric nanocomposite formed of BaTiO₃ nanoparticles and a smectic liquid crystal matrix. *Phase Transit.* **2010**, *83*, 1037–1047. [[CrossRef](#)]
23. Fatuzzo, E.; Harbeke, G.; Merz, W.J.; Nitsche, R.; Roetschi, H.; Ruppel, W. Ferroelectricity in SbSI. *Phys. Rev.* **1962**, *127*, 2036. [[CrossRef](#)]
24. Imai, K.; Kawada, S.; Ida, M. Anomalous Pyroelectric Properties of SbSI Single Crystals. *J. Phys. Soc. Jpn.* **1966**, *21*, 1855–1860. [[CrossRef](#)]
25. Bhalla, A.S.; Newnham, R.E.; Cross, L.E.; Dougherty, J.P.; Smith, W.A. Pyroelectricity in SbSI. *Ferroelectrics* **1981**, *33*, 3–7. [[CrossRef](#)]
26. Rao, T.S.; Mansingh, A. Electrical and Optical Properties of SbSI Films. *Jpn. J. Appl. Phys.* **1985**, *24*, 422. [[CrossRef](#)]
27. Narayanan, S.; Pandey, R.K. Physical vapor deposition of antimony sulpho-iodide (SbSI) thin films and their properties. In Proceedings of the 1994 IEEE International Symposium on Applications of Ferroelectrics, State College, PA, USA, 12–16 May 2014; IEEE: Piscataway, NJ, USA, 1994; pp. 309–311. [[CrossRef](#)]
28. Purusothaman, Y.; Alluri, N.R.; Chandrasekhar, A.; Kim, S.-J. Photoactive piezoelectric energy harvester driven by antimony sulfoiodide (SbSI): A A^{VB}V^{IC}V^{II} class ferroelectric-semiconductor compound. *Nano Energy* **2018**, *50*, 256–265. [[CrossRef](#)]
29. Toroń, B.; Mistewicz, K.; Jesionek, M.; Koziół, M.; Stróż, D.; Zubko, M. Nanogenerator for dynamic stimuli detection and mechanical energy harvesting based on compressed SbSeI nanowires. *Energy* **2020**, *212*, 118717. [[CrossRef](#)]
30. Mistewicz, K.; Jesionek, M.; Kim, H.J.; Hajra, S.; Koziół, M.; Chrobok, Ł.; Wang, X. Nanogenerator for determination of acoustic power in ultrasonic reactors. *Ultrason. Sonochem.* **2021**, *78*, 105718. [[CrossRef](#)]
31. Nie, R.; Yun, H.-S.; Paik, M.-J.; Mehta, A.; Park, B.-W.; Choi, Y.C.; Seok, S.I. Efficient Solar Cells Based on Light-Harvesting Antimony Sulfoiodide. *Adv. Energy Mater.* **2018**, *8*, 1701901. [[CrossRef](#)]
32. Mistewicz, K.; Matysiak, W.; Jesionek, M.; Jarka, P.; Kępińska, M.; Nowak, M.; Tański, T.; Stróż, D.; Szade, J.; Balin, K.; et al. A simple route for manufacture of photovoltaic devices based on chalcogenide nanowires. *Appl. Surf. Sci.* **2020**, *517*, 146138. [[CrossRef](#)]
33. Wang, C.; Zhang, M.; Fang, Y.; Chen, G.; Li, Q.; Sheng, X.; Xu, X.; Hui, J.; Lan, Y.; Fang, M.; et al. SbSI Nanocrystals: An Excellent Visible Light Photocatalyst with Efficient Generation of Singlet Oxygen. *ACS Sustain. Chem. Eng.* **2018**, *6*, 12166–12175. [[CrossRef](#)]
34. Mistewicz, K.; Kępińska, M.; Nowak, M.; Sasiela, A.; Zubko, M.; Stróż, D. Fast and Efficient Piezo/Photocatalytic Removal of Methyl Orange Using SbSI Nanowires. *Materials* **2020**, *13*, 4803. [[CrossRef](#)] [[PubMed](#)]
35. Yoshida, M.; Yamanaka, K.; Hamakawa, Y. Semiconducting and Dielectric Properties of C-Axis Oriented SbSI Thin Film. *Jpn. J. Appl. Phys.* **1973**, *12*, 1699. [[CrossRef](#)]
36. Mansingh, A.; Sudersena Rao, T. Growth and characterization of flash evaporated ferroelectric antimony sulphoiodide thin films. *J. Appl. Phys.* **1985**, *58*, 3530–3535. [[CrossRef](#)]
37. Mansingh, A.; Rao, T.S. I-V and C-V characteristics of ferroelectric SbSI (film)-Si-metal. *Ferroelectrics* **1983**, *50*, 263–264. [[CrossRef](#)]
38. Surthi, S.; Kotru, S.; Pandey, R.K. Preparation and electrical properties of ferroelectric SbSI films by pulsed laser deposition. *J. Mater. Sci. Lett.* **2003**, *22*, 591–593. [[CrossRef](#)]
39. Surthi, S.; Kotru, S.; Pandey, R.K. SbSI Films for Ferroelectric Memory Applications. *Integr. Ferroelectr.* **2002**, *48*, 263–269. [[CrossRef](#)]
40. Inagaki, S.; Nakamura, M.; Hatada, H.; Nishino, R.; Kagawa, F.; Tokura, Y.; Kawasaki, M. Growth of visible-light-responsive ferroelectric SbSI thin films by molecular beam epitaxy. *Appl. Phys. Lett.* **2020**, *116*, 072902. [[CrossRef](#)]
41. Choi, Y.C.; Hwang, E.; Kim, D.-H. Controlled growth of SbSI thin films from amorphous Sb₂S₃ for low-temperature solution processed chalcogenide solar cells. *APL Mater.* **2018**, *6*, 121108. [[CrossRef](#)]
42. Nie, R.; Seok, S.I. Efficient Antimony-Based Solar Cells by Enhanced Charge Transfer. *Small Methods* **2020**, *4*, 1900698. [[CrossRef](#)]
43. Gödel, K.C.; Steiner, U. Thin film synthesis of SbSI micro-crystals for self-powered photodetectors with rapid time response. *Nanoscale* **2016**, *8*, 15920–15925. [[CrossRef](#)]
44. Ye, H.; Xu, Y.; Mackenzie, J.D. Semiconducting ferroelectric SbSI quantum dots in organically modified TiO₂ matrix. In *Sol-Gel Optics V*; International Society for Optics and Photonics: Bellingham, WA, USA, 2000; Volume 3943, pp. 95–101. [[CrossRef](#)]
45. Gan, W.C.; Abd Majid, W.H. Effect of TiO₂ on enhanced pyroelectric activity of PVDF composite. *Smart Mater. Struct.* **2014**, *23*, 045026. [[CrossRef](#)]
46. Mistewicz, K.; Nowak, M.; Starczewska, A.; Jesionek, M.; Rzychoń, T.; Wrzalik, R.; Guiseppi-Elie, A. Determination of electrical conductivity type of SbSI nanowires. *Mater. Lett.* **2016**, *182*, 78–80. [[CrossRef](#)]
47. Zhang, M.; Hu, Q.; Ma, K.; Ding, Y.; Li, C. Pyroelectric effect in CdS nanorods decorated with a molecular Co-catalyst for hydrogen evolution. *Nano Energy* **2020**, *73*, 104810. [[CrossRef](#)]

48. Hu, J.; Liu, Q.; Zhang, H.; Chen, C.-D.; Liang, Y.; Du, R.-G.; Lin, C.-J. Facile ultrasonic deposition of SnO₂ nanoparticles on TiO₂ nanotube films for enhanced photoelectrochemical performances. *J. Mater. Chem. A* **2015**, *3*, 22605–22613. [[CrossRef](#)]
49. Zhang, Q.; Li, C. High Temperature Stable Anatase Phase Titanium Dioxide Films Synthesized by Mist Chemical Vapor Deposition. *Nanomaterials* **2020**, *10*, 911. [[CrossRef](#)] [[PubMed](#)]
50. Borchert, J.W.; Stewart, I.E.; Ye, S.; Rathmell, A.R.; Wiley, B.J.; Winey, K.I. Effects of length dispersity and film fabrication on the sheet resistance of copper nanowire transparent conductors. *Nanoscale* **2015**, *7*, 14496–14504. [[CrossRef](#)]
51. Khanarian, G.; Joo, J.; Liu, X.-Q.; Eastman, P.; Werner, D.; O'Connell, K.; Trefonas, P. The optical and electrical properties of silver nanowire mesh films. *J. Appl. Phys.* **2013**, *114*, 024302. [[CrossRef](#)]
52. Lu, C. On the bending strength of ZnO nanowires. *Phys. Lett. A* **2008**, *372*, 6113–6115. [[CrossRef](#)]
53. Yu, S.-P.; Liu, Y.-H.; Sun, A.-C.; Hsu, J.-H. Determining the size distribution of magnetic nanoparticles based on analysis of magnetization curves. *J. Appl. Phys.* **2009**, *106*, 103905. [[CrossRef](#)]
54. Pauw, B.R.; Kastner, C.; Thunemann, A.F. Nanoparticle size distribution quantification: Results of a small-angle X-ray scattering inter-laboratory comparison. *J. Appl. Cryst.* **2017**, *50*, 1280–1288. [[CrossRef](#)]
55. Wu, B.-K.; Chern, M.-Y.; Lee, H.-Y. Size-controllable synthesis and bandgap modulation of single-layered RF-sputtered bismuth nanoparticles. *Nanoscale Res. Lett.* **2014**, *9*, 249. [[CrossRef](#)] [[PubMed](#)]
56. Bochenek, D.; Niemiec, P.; Skulski, R.; Adamczyk, M.; Brzezińska, D. Electrophysical properties of the multicomponent PBZT-type ceramics doped by Sn⁴⁺. *J. Electroceram.* **2019**, *42*, 17–30. [[CrossRef](#)]
57. Dhananjay, D.; Nagaraju, N.; Krupanidhi, S.B. Off-centered polarization and ferroelectric phase transition in Li-doped ZnO thin films grown by pulsed-laser ablation. *J. Appl. Phys.* **2007**, *101*, 104104. [[CrossRef](#)]
58. Mansingh, A.; Srivastava, K.N.; Singh, B. Effect of surface capacitance on the dielectric behavior of ferroelectric lead germanate. *J. Appl. Phys.* **1979**, *50*, 4319. [[CrossRef](#)]
59. Połomska, M.; Hilczer, B.; Michalczyk, M. Electric conductivity of some ferroelectric crystals. *Ferroelectrics* **1981**, *39*, 1217–1220. [[CrossRef](#)]
60. Goto, Y.; Sawaguchi, E. Electric Conductivity of Ferroelectric Pb₅Ge₃O₁₁. *J. Phys. Soc. Jpn.* **1979**, *46*, 1580–1582. [[CrossRef](#)]
61. Rao, T.S.; Mansingh, A. Electrical properties of antimony sulphoiodide (SbSI) thin films. *Ferroelectrics* **1989**, *93*, 53. [[CrossRef](#)]
62. Mistewicz, K.; Nowak, M.; Stróż, D. A Ferroelectric-Photovoltaic Effect in SbSI Nanowires. *Nanomaterials* **2019**, *9*, 580. [[CrossRef](#)] [[PubMed](#)]
63. Tan, K.S.; Gan, W.C.; Velayutham, T.S.; Abd Majid, W.H. Pyroelectricity enhancement of PVDF nanocomposite thin films doped with ZnO nanoparticles. *Smart Mater. Struct.* **2014**, *23*, 125006. [[CrossRef](#)]
64. Mahdi, R.I.; Gan, W.C.; Halim, N.A.; Velayutham, T.S.; Abd Majid, W.H. Ferroelectric and pyroelectric properties of novel lead-free polyvinylidene fluoride-trifluoroethylene–Bi_{0.5}Na_{0.5}TiO₃ nanocomposite thin films for sensing applications. *Ceram. Int.* **2015**, *41*, 13836–13843. [[CrossRef](#)]
65. Mahdi, R.I.; Gan, W.C.; Abd Majid, W.H. Hot Plate Annealing at a Low Temperature of a Thin Ferroelectric P(VDF-TrFE) Film with an Improved Crystalline Structure for Sensors and Actuators. *Sensors* **2014**, *14*, 19115–19127. [[CrossRef](#)] [[PubMed](#)]
66. Krause, M.; Graz, I.; Bauer-Gogonea, S.; Bauer, S.; Ploss, B.; Zirkl, M.; Stadlober, B.; Helbig, U. PbTiO₃—P(VDF-TrFE)—Nanocomposites for Pressure and Temperature Sensitive Skin. *Ferroelectrics* **2011**, *419*, 23–27. [[CrossRef](#)]
67. Zhang, F.; Kang, H.; Lin, Y.; Guan, L.; Aslan, H.; Zhang, M.; Niu, L.; Dong, M. Studying the Pyroelectric Effects of LiNbO₃ Modified Composites. *Nanoscale Res. Lett.* **2020**, *15*, 106. [[CrossRef](#)] [[PubMed](#)]
68. Halim, N.A.; Abd Majid, W.H.; Velayutham, T.S. Ferroelectric, pyroelectric and piezoelectric properties of CeO₂-doped Na_{0.5}Bi_{0.5}TiO₃ ceramics. *SN Appl. Sci.* **2019**, *1*, 582. [[CrossRef](#)]
69. Sharma, A.P.; Behera, M.K.; Pradhan, D.K.; Pradhan, S.K.; Bonner, C.E.; Bahoura, M. Lead-free relaxor-ferroelectric thin films for energy harvesting from low-grade waste-heat. *Sci. Rep.* **2021**, *11*, 111. [[CrossRef](#)]
70. Xue, D.; Gao, J.; Zhang, L.; Bao, H.; Liu, W.; Zhou, C.; Ren, X. Aging effect in paraelectric state of ferroelectrics: Implication for a microscopic explanation of ferroelectric deaging. *Appl. Phys. Lett.* **2009**, *94*, 082902. [[CrossRef](#)]
71. Nakamura, M.; Hatada, H.; Kaneko, Y.; Ogawa, N.; Sotome, M.; Tokura, Y.; Kawasaki, M. Non-local photocurrent in a ferroelectric semiconductor SbSI under local photoexcitation. *Appl. Phys. Lett.* **2020**, *116*, 122902. [[CrossRef](#)]
72. Nakamura, M.; Hatada, H.; Kaneko, Y.; Ogawa, N.; Tokura, Y.; Kawasaki, M. Impact of electrodes on the extraction of shift current from a ferroelectric semiconductor SbSI. *Appl. Phys. Lett.* **2018**, *113*, 232901. [[CrossRef](#)]
73. Yu, Z.; Perera, I.R.; Daeneke, T.; Makuta, S.; Tachibana, Y.; Jasieniak, J.J.; Mishra, A.; Bäuerle, P.; Spiccia, L.; Bach, U. Indium tin oxide as a semiconductor material in efficient p-type dye-sensitized solar cells. *NPG Asia Mater.* **2016**, *8*, e305. [[CrossRef](#)]
74. Anitha, V.C.; Banerjee, A.N.; Joo, S.W. Recent developments in TiO₂ as n- and p-type transparent semiconductors: Synthesis, modification, properties, and energy related applications. *J. Mater. Sci.* **2015**, *50*, 7495–7536. [[CrossRef](#)]
75. Park, Y.; Choong, V.; Gao, Y.; Hsieh, B.R.; Tang, C.W. Work function of indium tin oxide transparent conductor measured by photoelectron spectroscopy. *Appl. Phys. Lett.* **1996**, *68*, 2699. [[CrossRef](#)]
76. Mansfeldova, V.; Zlamalova, M.; Tarabkova, H.; Janda, P.; Vorokhta, M.; Piliat, L.; Kavan, L. Work Function of TiO₂ (Anatase, Rutile, and Brookite) Single Crystals: Effects of the Environment. *J. Phys. Chem. C* **2021**, *125*, 1902–1912. [[CrossRef](#)]
77. Wang, X.; Song, J.; Liu, J.; Wang, Z.L. Direct-Current Nanogenerator Driven by Ultrasonic Waves. *Science* **2007**, *316*, 102–105. [[CrossRef](#)]

78. Yang, R.; Xu, R.; Dou, W.; Benner, M.; Zhang, Q.; Liu, J. Semiconductor-based dynamic heterojunctions as an emerging strategy for high direct-current mechanical energy harvesting. *Nano Energy* **2021**, *83*, 105849. [[CrossRef](#)]
79. Lu, Y.; Hao, Z.; Feng, S.; Shen, R.; Yan, Y.; Lin, S. Direct-Current Generator Based on Dynamic PN Junctions with the Designed Voltage Output. *iScience* **2019**, *22*, 58–69. [[CrossRef](#)]
80. Liu, J.; Liu, F.; Bao, R.; Jiang, K.; Khan, F.; Li, Z.; Peng, H.; Chen, J.; Alodhayb, A.; Thundat, T. Scaled-up Direct-Current Generation in MoS₂ Multilayer-Based Moving Heterojunctions. *ACS Appl. Mater. Interfaces* **2019**, *11*, 35404–35409. [[CrossRef](#)]
81. Lu, Y.; Yan, Y.; Yu, X.; Zhou, X.; Feng, S.; Xu, C.; Zheng, H.; Yang, Z.; Li, L.; Liu, K.; et al. Polarized Water Driven Dynamic PN Junction-Based Direct-Current Generator. *Research* **2021**, *2021*, 7505638. [[CrossRef](#)]
82. Meng, J.; Guo, Z.H.; Pan, C.; Wang, L.; Chang, C.; Li, L.; Pu, X.; Wang, Z.L. Flexible Textile Direct-Current Generator Based on the Tribovoltaic Effect at Dynamic Metal-Semiconducting Polymer Interfaces. *ACS Energy Lett.* **2021**, *6*, 2442–2450. [[CrossRef](#)]
83. Wang, W.; Han, X.; Niu, J.; Jin, X.; Wang, H.; Shao, H.; Lin, T. Direct-current energy generators from polypyrrole-coated fabric/metal Schottky diodes with considerably improved output. *J. Mater. Chem. A* **2020**, *8*, 24166–24174. [[CrossRef](#)]
84. Ding, X.; Shao, H.; Wang, H.; Yang, W.; Fang, J.; Zhang, D.; Lin, T. Schottky DC generators with considerable enhanced power output and energy conversion efficiency based on polypyrrole-TiO₂ nanocomposite. *Nano Energy* **2021**, *89*, 106367. [[CrossRef](#)]
85. Shao, H.; Fang, J.; Wang, H.; Zhou, H.; Lin, T. Direct current energy generators from a conducting polymer–inorganic oxide junction. *J. Mater. Chem. A* **2017**, *5*, 8267–8273. [[CrossRef](#)]
86. Sandomirsky, V.; Schlesinger, Y.; Dashevsky, Z. Pyroelectric effect of a p–n junction in a nonpolar solid. *Appl. Phys. Lett.* **2005**, *86*, 133501. [[CrossRef](#)]
87. Mistewicz, K.; Jesionek, M.; Nowak, M.; Kozioł, M. SbSeI pyroelectric nanogenerator for a low temperature waste heat recovery. *Nano Energy* **2019**, *64*, 103906. [[CrossRef](#)]
88. Grigas, J.; Talik, E.; Adamiec, M.; Lazauskas, V. X-ray photoelectron spectra and electronic structure of quasi-one-dimensional SbSeI crystals. *Condens. Matter Phys.* **2007**, *10*, 101–110. [[CrossRef](#)]
89. Suyal, G.; Seifert, A.; Setter, N. Pyroelectric nanoporous films: Synthesis and properties. *Appl. Phys. Lett.* **2002**, *81*, 1059. [[CrossRef](#)]
90. Seifert, A.; Sagalowicz, L.; Murali, P.; Setter, N. Microstructural evolution of dense and porous pyroelectric Pb_{1–ax}CaxTiO₃ thin films. *J. Mater. Res.* **1999**, *14*, 2012–2022. [[CrossRef](#)]
91. Yang, Y.; Guo, W.; Pradel, K.C.; Zhu, G.; Zhou, Y.; Zhang, Y.; Hu, Y.; Lin, L.; Wang, Z.L. Pyroelectric Nanogenerators for Harvesting Thermoelectric Energy. *Nano Lett.* **2012**, *12*, 2833–2838. [[CrossRef](#)]
92. Bukowski, T.J.; McCarthy, K.; McCarthy, F.; Teowee, G.; Alexander, T.P.; Uhlmann, D.R.; Dawley, J.T.; Zelinski, B.J.J. Piezoelectric properties of sol-gel derived ZnO thin films. *Integr. Ferroelectr.* **1997**, *17*, 339–347. [[CrossRef](#)]
93. Zhang, K.; Wang, Y.; Wang, Z.L.; Yang, Y. Standard and figure-of-merit for quantifying the performance of pyroelectric nanogenerators. *Nano Energy* **2019**, *55*, 534–540. [[CrossRef](#)]
94. Saito, T.; Kawai, Y.; Ono, T. Thermoelectric power generator based on a ferroelectric material combined with a bimetal thermostat. In *Transducers & Eurosensors XXVII, Proceedings of the 17th International Conference on Solid-State Sensors, Actuators and Microsystems, Barcelona, Spain, 16–20 June 2013*; IEEE: Piscataway, NJ, USA, 2013; pp. 2280–2283. [[CrossRef](#)]
95. Narita, F.; Fox, M.; Mori, K.; Takeuchi, H.; Kobayashi, T.; Omote, K. Potential of energy harvesting in barium titanate based laminates from room temperature to cryogenic/high temperatures: Measurements and linking phase field and finite element simulations. *Smart Mater. Struct.* **2017**, *26*, 115027. [[CrossRef](#)]
96. Zhao, K.; Ouyang, B.; Yang, Y. Enhancing Photocurrent of Radially Polarized Ferroelectric BaTiO₃ Materials by Ferro-Pyro-Phototronic Effect. *iScience* **2018**, *3*, 208–216. [[CrossRef](#)] [[PubMed](#)]
97. Karim, H.; Sarker, M.R.H.; Shahriar, S.; Shuvo, M.A.I.; Delfin, D.; Hodges, D.; Tseng, T.-L.; Roberson, D.; Love, N.; Lin, Y. Feasibility study of thermal energy harvesting using lead free pyroelectrics. *Smart Mater. Struct.* **2016**, *25*, 055022. [[CrossRef](#)]
98. Zhao, T.; Jiang, W.; Liu, H.; Niu, D.; Li, X.; Liu, W.; Li, X.; Chen, B.; Shi, Y.; Yin, L.; et al. An infrared-driven flexible pyroelectric generator for non-contact energy harvester. *Nanoscale* **2016**, *8*, 8111–8117. [[CrossRef](#)] [[PubMed](#)]
99. You, M.-H.; Wang, X.-X.; Yan, X.; Zhang, J.; Song, W.-Z.; Yu, M.; Fan, Z.-Y.; Ramakrishna, S.; Long, Y.-Z. A self-powered flexible hybrid piezoelectric–pyroelectric nanogenerator based on non-woven nanofiber membranes. *J. Mater. Chem. A* **2018**, *6*, 3500–3509. [[CrossRef](#)]
100. Kim, J.; Lee, J.H.; Ryu, H.; Lee, J.-H.; Khan, U.; Kim, H.; Kwak, S.S.; Kim, S.-W. High-Performance Piezoelectric, Pyroelectric, and Triboelectric Nanogenerators Based on P(VDF-TrFE) with Controlled Crystallinity and Dipole Alignment. *Adv. Funct. Mater.* **2017**, *27*, 1700702. [[CrossRef](#)]
101. Mascot, M.; Fasquelle, D.; Velu, G.; Ferri, A.; Desfeux, R.; Courcot, L.; Carru, J.C. Pyro, Ferro and Dielectric Properties of Ba_{0.8}Sr_{0.2}TiO₃ Films Deposited by Sol-Gel on Platinized Silicon Substrates. *Ferroelectrics* **2008**, *362*, 79–86. [[CrossRef](#)]
102. Yang, Y.; Jung, J.H.; Yun, B.K.; Zhang, F.; Pradel, K.C.; Guo, W.; Wang, Z.L. Flexible Pyroelectric Nanogenerators using a Composite Structure of Lead-Free KNbO₃ Nanowires. *Adv. Mater.* **2012**, *24*, 5357–5362. [[CrossRef](#)]
103. Olszowy, M.; Pawlaczyk, C.; Markiewicz, E.; Kulek, J. Dielectric and pyroelectric properties of BaTiO₃–PVC composites. *Phys. Stat. Sol. A* **2005**, *202*, 1848–1853. [[CrossRef](#)]
104. Li, W.; Zheng, A.; Lin, Y.; Liu, P.; Shen, M.; Zhou, L.; Liu, H.; Yuan, J.; Qin, S.; Zhang, X.; et al. High pyroelectric effect in poly(vinylidene fluoride) composites cooperated with diamond nanoparticles. *Mater. Lett.* **2020**, *267*, 127514. [[CrossRef](#)]

105. Sultana, A.; Ghosh, S.K.; Alam, M.M.; Sadhukhan, P.; Roy, K.; Xie, M.; Bowen, C.R.; Sarkar, S.; Das, S.; Middy, T.R.; et al. Methylammonium Lead Iodide Incorporated Poly(vinylidene fluoride) Nanofibers for Flexible Piezoelectric–Pyroelectric Nanogenerator. *ACS Appl. Mater. Interfaces* **2019**, *11*, 27279–27287. [[CrossRef](#)] [[PubMed](#)]
106. Avinash, B.S.; Chaturmukha, V.S.; Jayanna, H.S.; Naveen, C.S.; Rajeeva, M.P.; Harish, B.M.; Suresh, S.; Lamani, A.R. Effect of particle size on band gap and DC electrical conductivity of TiO₂ nanomaterial. In *AIP Conference Proceedings*; AIP Publishing LLC.: Melville, NY, USA, 2016; Volume 1728, p. 020426. [[CrossRef](#)]
107. Wei, N.; Zhang, D.-M.; Yang, F.-X.; Han, X.-Y.; Zhong, Z.-C.; Zheng, K.-Y. Effect of electrical conductivity on the polarization behaviour and pyroelectric, piezoelectric property prediction of 0–3 ferroelectric composites. *J. Phys. Appl. Phys.* **2007**, *40*, 2716–2722. [[CrossRef](#)]